



EFFECTS OF FIELD-LINE TOPOLOGY ON ENERGY PROPAGATION IN THE CORONA

S. CANDELARESI, D. I. PONTIN, AND G. HORNIG

Division of Mathematics, University of Dundee, Dundee, DD1 4HN, UK

Received 2016 July 9; revised 2016 September 20; accepted 2016 September 23; published 2016 November 29

ABSTRACT

We study the effect of photospheric footpoint motions on magnetic field structures containing magnetic nulls. The footpoint motions are prescribed on the photospheric boundary as a velocity field that entangles the magnetic field. We investigate the propagation of the injected energy, the conversion of energy, emergence of current layers, and other consequences of the nontrivial magnetic field topology in this situation. These boundary motions lead initially to an increase in magnetic and kinetic energy. Following this, the energy input from the photosphere is partially dissipated and partially transported out of the domain through the Poynting flux. The presence of separatrix layers and magnetic null points fundamentally alters the propagation behavior of disturbances from the photosphere into the corona. Depending on the field-line topology close to the photosphere, the energy is either trapped or free to propagate into the corona.

Key words: magnetic reconnection – magnetohydrodynamics (MHD) – plasmas – Sun: magnetic fields – Sun: photosphere – sunspots

Supporting material: animations

1. INTRODUCTION

From observations and field extrapolations (e.g., Longcope et al. 2003; Platten et al. 2014) we know that the solar magnetic field has a rather complex structure. Apart from its solar-scale toroidal and poloidal field, which is rather weak compared to small-scale contributions, there are large-scale magnetic field lines connecting back to the photosphere (e.g., Filippov 1999) that are anchored at magnetic footpoints. Such large-scale loops are found both inside and outside active regions (Larmor 1934; Gošić et al. 2014).

Magnetic field structures exist also on much smaller scales, and we now know that the lower corona is characterized by a so-called magnetic carpet structure of many short, differently oriented loops due to mixed polarities of opposite signs over a broad range of scales (e.g., Schrijver et al. 1998). Such fields contain a large number of magnetic null points with a decreasing population density with height (Longcope et al. 2003; Edwards & Parnell 2015). The presence of these null points and the wide range of field-line topologies in general—from short low-lying loops to long loops that extend high into the atmosphere and open field lines—are essential in understanding the propagation of energy from footpoint motions (e.g., Filippov 1999; Schrijver et al. 2010; Santamaria et al. 2015) to the upper layers of the solar atmosphere.

It is now well established that various geometrical or topological features of the coronal magnetic field are preferential sites for current accumulation and magnetic reconnection (Lau & Finn 1990; Bogdanov et al. 1994; Démoulin et al. 1997; Aulanier et al. 2005; Pontin & Craig 2005; Pontin et al. 2007; Effenberger & Craig 2015). Such features include magnetic null points and their associated separatrix surfaces, separator lines (intersections of these separatrix surfaces), and quasi-separatrix layers (see Pontin 2011, and references therein). Together the magnetic null points and associated separatrix surfaces and separators are termed the “magnetic skeleton” of the field. Priest et al. (2002) have proposed that reconnection at these structures within the

Sun’s so-called magnetic carpet could provide an integral contribution to the heating of the coronal plasma.

In this paper we study the evolution of a coronal magnetic field of nontrivial topology under the influence of prescribed photospheric motions. There exist a number of previous studies dealing with such a scenario, following two main approaches. In the first, the full coronal system is simulated, and the overall behavior of the system is analyzed—such an approach has been successful in demonstrating heating of the coronal plasma for numerically accessible parameter regimes (e.g., Gudiksen & Nordlund 2005; Bingert & Peter 2011). The second approach involves using a much simpler model for the coronal field and plasma, but has the advantage that the detailed time evolution of the coronal field structure and energy distribution may be followed. Previous studies of this nature have focused on configurations in which the opposite magnetic polarities on the photosphere are well separated (e.g., Galsgaard et al. 2000; Mellor et al. 2005; De Moortel & Galsgaard 2006), and have demonstrated that reconnection and plasma heating take place. By contrast to these studies, here we consider the case in which the photospheric polarities are intermixed—as observed over a large portion of the photosphere—leading to configurations with magnetic nulls within the coronal volume.

In this work we investigate the effect of footpoint motions on the coronal magnetic field, in particular the propagation of energy and change in topology. Throughout this paper we refer to magnetic topology with respect to a reference field, as in the definition of the relative magnetic helicity. This implies that two fields only have equivalent topology if one can be transformed into the other by a smooth deformation that leaves the boundaries undisturbed. Therefore, the topology is distinguished not only by the distribution of magnetic null points and separatrix layers but also by magnetic-field-line braiding. Such braiding represents a nontrivial topology of the field since the field lines can only be “unbraided” by either performing motions on the boundary or allowing reconnection of field lines in the volume. It is expected that the topology plays a crucial role in the energy transport. We present three distinct initial fields and discuss their differences and

similarities. Finally, we conclude with drawing connections to the solar magnetic field.

2. MODEL AND METHODS

It is expected that the formation of electric current concentrations and propagation of energy in response to footpoint motions will vary greatly depending on the magnetic field topology. Therefore, we examine three magnetic field configurations as described in Section 2.1, while the fluid is driven using a prescribed driver at the lower z -boundary (see Section 2.6).

2.1. Setups

The initial magnetic field for all of the simulations is potential. Three different initial conditions are considered here. The first we use as a “control” case and simply consists of a homogeneous field in the z -direction, while the others contain magnetic null points and are referred to as magnetic carpet structures. They are constructed by positioning magnetic dipoles outside the physical domain. The field configurations are chosen such that some field lines close back to the lower boundary, hence creating a magnetic carpet-like structure. The three different initial conditions considered are described in turn below.

To simplify the setups, we choose an initially homogeneous density of value $\rho_0 = 1$ for all test cases and set the sound speed to $c_s = 1$. Since the magnetic field strength varies in space, the Alfvén speed changes as well with $v_A = |\mathbf{B}|/\sqrt{\mu_0\rho}$, with the magnetic field \mathbf{B} and the vacuum permeability μ_0 , which we set to 1.

2.1.1. Homogeneous Field

The homogeneous magnetic field is simply given by

$$\mathbf{B} = B_0 \hat{\mathbf{e}}_z, \quad (1)$$

where we choose $B_0 = 0.25$. Since the magnetohydrodynamics (MHD) code we apply for our simulations uses the magnetic vector potential, we need to express \mathbf{B} in terms of the magnetic vector potential \mathbf{A} with $\mathbf{B} = \nabla \times \mathbf{A}$:

$$\mathbf{A} = \frac{1}{2} B_0 \begin{pmatrix} -y \\ x \\ 0 \end{pmatrix}. \quad (2)$$

For this configuration the domain is chosen to be $-4 \leq x \leq 4$, $-4 \leq y \leq 4$, and $0 \leq z \leq 48$ with a spatial resolution of 256^3 grid points.

2.1.2. Embedded Parasitic Polarities

In the first mixed polarity case considered the photosphere consists of magnetic flux concentrations embedded within a weaker uniform polarity region of the opposite sign, such that the total flux of the uniform polarity dominates. Therefore, in this case the field at large distances along the loop has the same sign as this uniform background field, while the embedded photospheric magnetic flux concentrations of opposite sign constitute “parasitic polarity” regions. Above each of these parasitic polarities is a separatrix dome that encloses all of the flux that connects from the parasitic polarity back to the photosphere—distinguishing it from flux that connects from the photosphere up to the body of the loop (and the top boundary).

Some sample magnetic field lines are plotted in Figure 1, together with the magnetic skeleton that includes the separatrix surfaces.

The magnetic field is constructed by placing three magnetic dipoles at locations outside our domain of interest. Specifically, we restrict our studies to the half-space $z > 0$, where $z = 0$ represents the photosphere, and place all dipoles at $z < 0$. The vector potential for this magnetic field is given by

$$\mathbf{A} = \mathbf{A}_0 + B_0 \sum_{i=1}^n \epsilon_i \frac{\mathbf{e}_z \times (\mathbf{x} - \mathbf{x}_i)}{|\mathbf{x} - \mathbf{x}_i|^3}, \quad (3)$$

where \mathbf{A}_0 is the background magnetic field from Equation (2), \mathbf{x}_i are the locations, and ϵ_i are the strengths of the dipoles. Here we take $n = 3$, $\epsilon_{1,2,3} = -2$, $\mathbf{x}_1 = (0, 0, -0.85)$, $\mathbf{x}_2 = (2, 0, -0.85)$, $\mathbf{x}_3 = (-2, 0, -0.85)$, and $B_0 = 0.1$. To make the field quasi-periodic at the x and y boundaries (and thus ensure that the field lines within the loop are approximately tangent to these boundaries), we also add mirror dipoles in the eight squares surrounding the computational domain in x and y , also at $z = -0.85$. The domain extends for this configuration to $-4 \leq x \leq 4$, $-4 \leq y \leq 4$, and $0 \leq z \leq 16$ with a spatial resolution of $256 \times 256 \times 512$ grid points.

2.1.3. Embedded Dominant Polarities

As a contrast to the above parasitic polarity case, we also run simulations in which the embedded localized polarity regions form the flux of the loop (requiring that the total flux through the photosphere in our domain of interest is dominated by these polarities). We refer to this case as embedded dominant polarities. As shown in Figure 2, this results in the field lines taking on the classic “wine glass” shape. As shown in the right panel of Figure 2, the magnetic field in this case also contains magnetic null points, but in this case the associated separatrix surfaces do not close over regions of the photosphere, but rather extend vertically along the length of the loop, separating the flux associated with each embedded dominant polarity, in a manner reminiscent of the *coronal tectonics* model of Priest et al. (2002).

The magnetic field setup that we use is again defined by Equation (3), this time with parameters as follows: $n = 3$, $\epsilon_{1,2,3} = 0.3$, $\mathbf{x}_1 = (0, 0, -0.3)$, $\mathbf{x}_2 = (2.5, 0, -0.3)$, $\mathbf{x}_3 = (-2.5, 0, -0.3)$, and $B_0 = 0.1$. Similarly to the parasitic polarity setup, we place mirror dipoles below the eight squares surrounding the computational domain in the xy -plane. We also choose the same domain size as previously, specifically $-4 \leq x \leq 4$, $-4 \leq y \leq 4$, and $0 \leq z \leq 16$ with a spatial resolution of $240 \times 240 \times 480$ grid points.

2.2. Numerical Setup

In order to capture the full effects of magnetic diffusion and reconnection, we solve for the evolution of our magnetized fluid under the full MHD equations for a resistive, viscous, isothermal, and compressible gas:

$$\frac{\partial \mathbf{A}}{\partial t} = \mathbf{u} \times \mathbf{B} + \eta \nabla^2 \mathbf{A}, \quad (4)$$

$$\frac{D\mathbf{u}}{Dt} = -c_s^2 \nabla \ln \rho + \mathbf{J} \times \mathbf{B} / \rho + \mathbf{F}_{\text{visc}}, \quad (5)$$

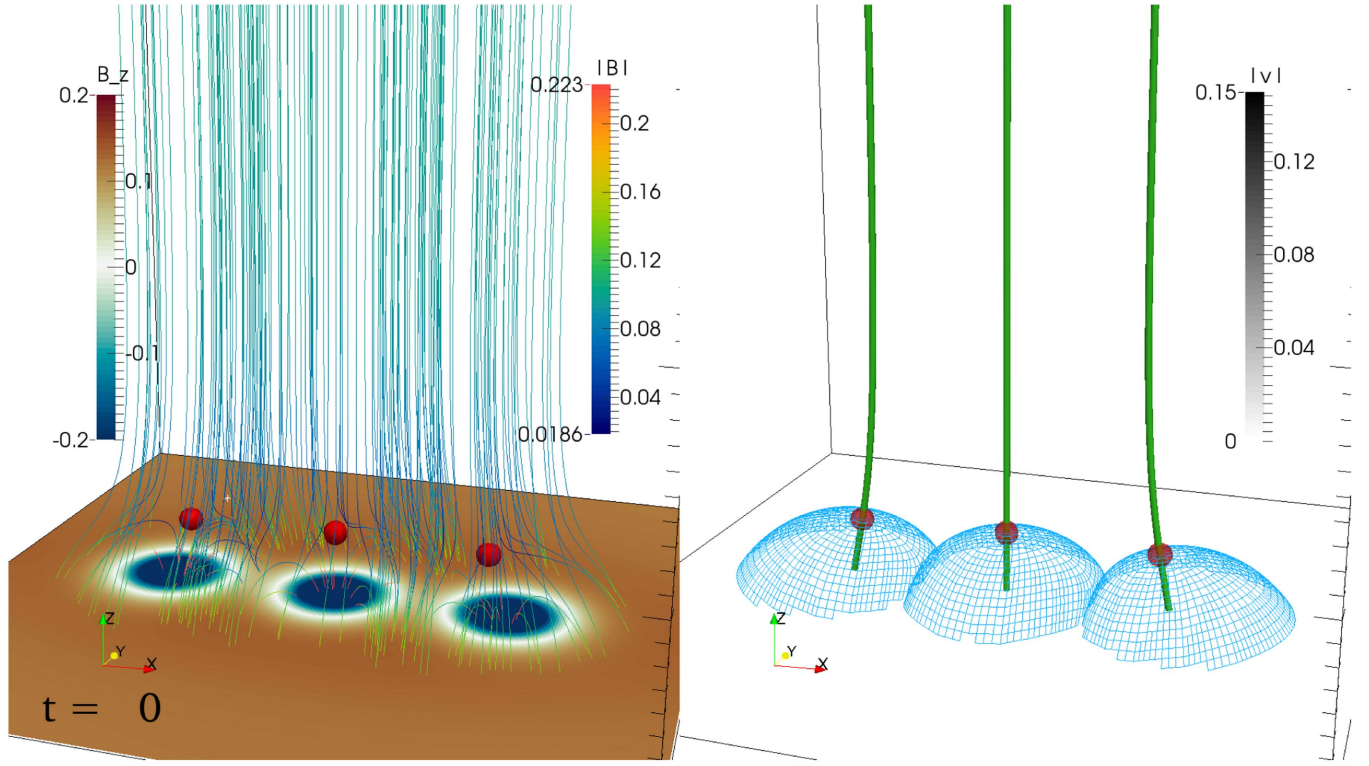


Figure 1. Initial condition for the embedded parasitic polarities. The field lines in the left panel are tracing the magnetic field, where the color denotes the strength of the magnetic field, the red spheres mark the locations of the magnetic nulls, and the color at the lower boundary denotes the z -component of the magnetic field. The right panel also shows the magnetic nulls together with the separatrix surfaces as a blue wire frame and the magnetic spines as green tubes. (The time evolution of this configuration is available as an animation.)

(An animation of this figure is available.)

$$\frac{D \ln \rho}{Dt} = -\nabla \cdot \mathbf{u}, \quad (6)$$

with the magnetic vector potential \mathbf{A} , velocity \mathbf{u} , magnetic field $\mathbf{B} = \nabla \times \mathbf{A}$, magnetic resistivity η , isothermal speed of sound c_s , density ρ , current density $\mathbf{J} = \nabla \times \mathbf{B}$, viscous forces \mathbf{F}_{visc} , and Lagrangian time derivative $D/Dt = \partial/\partial t + \mathbf{u} \cdot \nabla$. Here the viscous forces are given as $\mathbf{F}_{\text{visc}} = \rho^{-1} \nabla \cdot 2\nu\rho\mathbf{S}$, with the kinematic viscosity ν and traceless rate of strain tensor $\mathbf{S}_{ij} = \frac{1}{2}(u_{ij} + u_{ji}) - \frac{1}{3}\delta_{ij}\nabla \cdot \mathbf{u}$. This being an isothermal gas, we have $p = c_s^2 \rho$ for the pressure. For the vector potential \mathbf{A} we apply the Weyl gauge with $\nabla \cdot \mathbf{A} = 0$.

Throughout our simulations we use $\eta = 4 \times 10^{-4}$ to reduce magnetic energy dissipation as much as the limited resolution allows. For the kinematic viscosity we choose $\nu = 10^{-4}$ for the homogeneous initial field and 4×10^{-3} for the other simulations. This is necessary to dissipate the stresses that build up in the vicinity of the lower boundary.

Equations (4)–(6) are solved using the PENCIL CODE, which is an Eulerian finite-difference code using sixth-order-in-space derivatives and a third-order time-stepping scheme (Brandenburg & Dobler 2002).

2.3. Boundary Conditions

Any flow through the side boundaries (x and y) and the lower boundary (z_0) is suppressed, as we set the normal component of the velocity field to zero, while the tangential component is free (derivative across the boundary is zero). For the upper

boundary the velocity can, in principle, reach any value, as we set all components antisymmetric with respect to the boundary value. On the lower boundary a tangential flow is prescribed, using the method described in Section 2.6.

The boundary conditions for the density are set to symmetric at all boundaries, which forces its derivative across the boundaries to zero, but does not directly restrict its value. With the isothermal equation of state, this implies that the pressure forces across the boundaries are zero.

For the magnetic field we set the x and y components of the vector potential to be antisymmetric with respect to the boundary value at the x and y boundaries, while the z -component is symmetric. This unusual condition is needed due to the presence of a mean magnetic field in the z -direction for which the vector potential increases linearly in magnitude with distance from the projected center. At the upper boundary we choose all three components of the magnetic vector potential to be antisymmetric with respect to the boundary value.

For the lower boundary we choose two different conditions, depending on the initial field, to ensure that any initially potential field is also potential, i.e., current-free, at the boundary. This is achieved by extrapolating the field into the ghost zones via a potential field extrapolation. For the homogeneous initial condition we choose the same conditions at z_0 for the magnetic vector potential as for the side boundaries. While the used extrapolation routine renders the parasitic polarity field to be potential to a good approximation at the lower boundary, for the dominant polarity case we observe a small “residue” nonpotentiality near $z = z_0$. This has

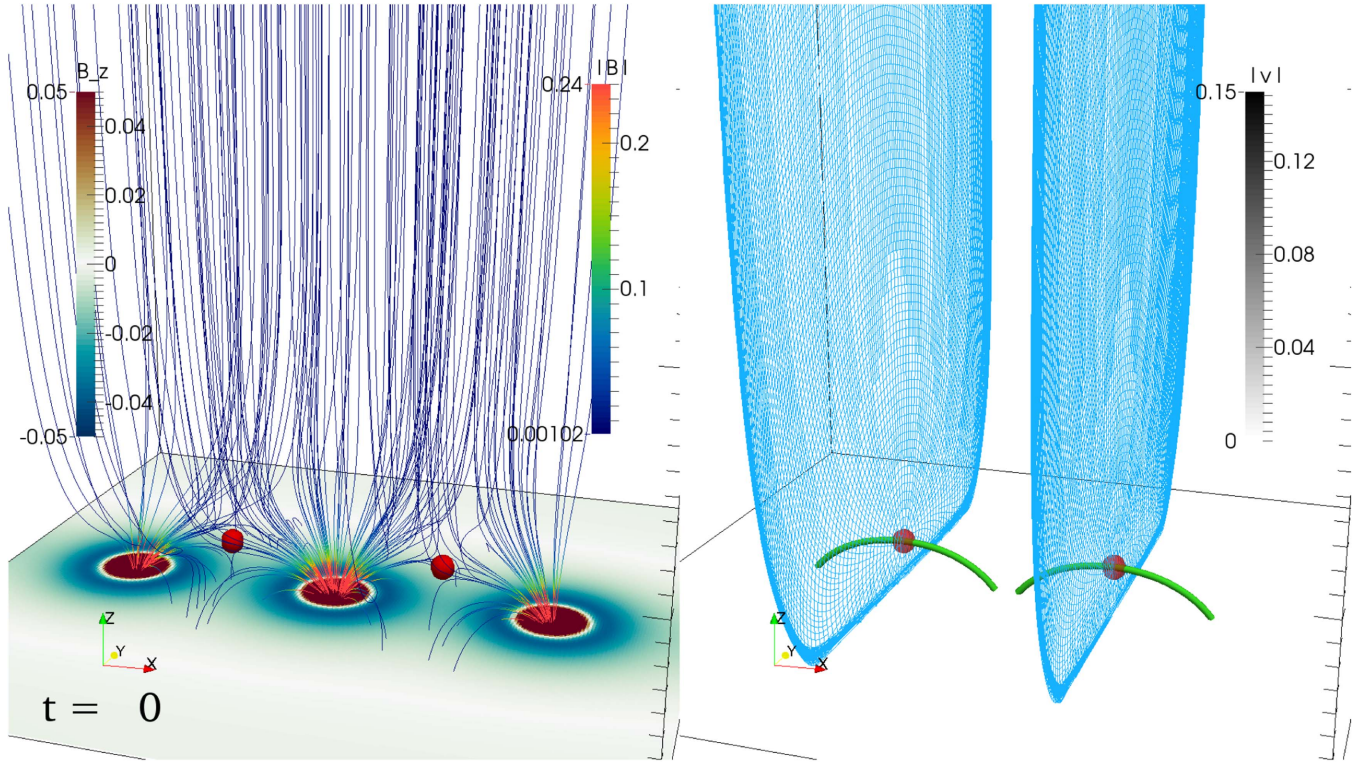


Figure 2. Initial condition for the embedded dominant polarities. The field lines in the left panel are tracing the magnetic field, where the color denotes the strength of the magnetic field, the red spheres mark the locations of the magnetic nulls, and the color at the lower boundary denotes the z -component of the magnetic field. The right panel also shows the magnetic nulls together with the separatrix surfaces as a blue wire frame and the magnetic spines as green tubes. (The time evolution of this configuration is available as an animation.)

(An animation of this figure is available.)

consequences for the field's initial dynamics before the system damps away those small deviations.

2.4. Wave Damping Region

We wish to simulate an upper boundary that is open for Alfvénic waves and to analyze the energy propagation into the corona without the complicating effects of reflection from the opposite loop footpoints. However, as specified, the upper boundary condition for the magnetic vector potential is such that Alfvénic waves reflect, rather than leave, the domain. This would lead to the interference of the upward- and downward-traveling waves with possible accumulation of magnetic energy in the domain. We therefore impose a wave damping region for the embedded and parasitic polarity configuration that extends from $z = 8$ to the top of the domain at $z = 16$, in which we increase the viscosity by a factor of 8 within an interval of length 1 at $z = 8$ via a step-like function via a hyperbolic tangent variation. As the reflected damped wave returns from the damping region, its intensity is only a fraction of what it was initially, which is typically less than 7.7% of the amplitude of the wave entering the damping region. Our subsequent energy dissipation and flux calculations are performed on the domain excluding the wave damping region. We omit the wave damping region for the homogeneous case, since we stop the simulation as soon as the first disturbance reaches the upper boundary.

2.5. Energy Dissipation and Fluxes

In our isothermal compressible system, kinetic energy and magnetic energy can be transformed into one another through the action of the Lorentz force; in addition, each may be dissipated by the resistive and viscous terms—this energy being lost to the system due to the isothermal assumption. Since the boundary conditions allow for magnetic energy fluxes out of the domain, we also need to take those into account when considering the overall energy balance.

2.5.1. Magnetic Energy

Starting from the induction Equation (4), we can derive the form for the magnetic energy variation as

$$\begin{aligned} \frac{d}{dt} E_M &= \frac{1}{2} \frac{d}{dt} \int_V \mathbf{B}^2 dV \\ &= \int_V \underbrace{(-\mathbf{J} \times \mathbf{B}) \cdot \mathbf{u}}_{\text{Lorentz}} - \underbrace{\eta \mathbf{J}^2}_{\text{Ohmic}} dV \\ &\quad + \int_{\partial V} \underbrace{((\mathbf{B} \cdot \mathbf{u})\mathbf{B} - \mathbf{B}^2 \mathbf{u} - \eta \mathbf{J} \times \mathbf{B}) \cdot \mathbf{n}}_{\text{fluxes}} dS, \end{aligned} \quad (7)$$

where the first integral is over the domain V , which excludes the wave damping region, and the second is a surface integral over the boundary ∂V , with normal vector \mathbf{n} pointing outside the domain and dS being the infinitesimal surface element on ∂V .

The different terms in Equation (7) are the work done by the Lorentz force, the ohmic dissipation, and the three flux terms at the boundaries, respectively. We will consider each of the five terms separately.

2.5.2. Kinetic Energy

Similar to the calculations for the magnetic energy, we can use the momentum Equation (5) and the continuity Equation (6) to compute the different terms for the kinetic energy flux and dissipation to obtain

$$\begin{aligned} \frac{d}{dt} E_K &= \frac{1}{2} \frac{d}{dt} \int_V \rho u^2 dV \\ &= \int_V \underbrace{-c_s^2 \mathbf{u} \cdot \nabla \rho}_{\text{compression}} + \underbrace{(\mathbf{J} \times \mathbf{B}) \cdot \mathbf{u}}_{\text{Lorentz}} + \underbrace{\rho \mathbf{u} \cdot \mathbf{F}_{\text{visc}}}_{\text{viscous}} dV \\ &\quad + \frac{1}{2} \int_{\partial V} \underbrace{-(\mathbf{u}^2 \rho \mathbf{u}) \cdot \mathbf{n} dS}_{\text{fluxes}}. \end{aligned} \quad (8)$$

The terms are the gas compression term through which kinetic energy is dissipated into heat (and lost from the system), the work done by the Lorentz force, which couples the magnetic field with the fluid, the viscous dissipation, and the fluxes through the boundaries, respectively. As with the magnetic energy, we will consider each of the four terms separately.

2.6. Boundary Driver

Photospheric footpoint motions are simulated by imposing a time- and space-varying velocity field at the lower ($z = z_0$) boundary. Any existing magnetic field that connects to this boundary is then subjected to this driving. For the driving velocities we prescribe a blinking vortex pattern, which, when applied on the boundary of an initially homogeneous magnetic field in an ideal fluid, would create the so-called E^3 braid of Wilmot-Smith et al. (2009). The evolution of the homogeneous field under continued application of such a boundary driving pattern was recently considered by Ritchie et al. (2016). The driving flow consists of two (partially overlapping) circular regions at which opposite twisting motions are applied. The timescale of the driver is such that within the time of the simulations a total of six twisting motions are applied at the photosphere (three of each sign). Specifically, we force the velocity at $z = z_0$ toward the following profile:

$$u_d^x(x, y, z_0) = \pm u_0 \exp[(-(x \mp x_c)^2 - y^2)/2 - (\text{mod}(t, t_{E3}))^2 / (t_{E3}/4)^2](-y) \quad (9)$$

$$u_d^y(x, y, z_0) = \pm u_0 k_c \exp[(-(x \mp x_c)^2 - y^2)/2 - (\text{mod}(t, t_{E3}))^2 / (t_{E3}/4)^2](x \mp x_c) \quad (10)$$

$$u_d^z(x, y, z_0) = 0. \quad (11)$$

Here we use $t_{E3} = 32$ and $x_c = 1$. Our choice of t_{E3} is motivated by the Alfvén travel time of 192 time units for our box of 48 in length and Alfvén speed of 0.25, which requires a cadence of 32 time units in order to fit six twist regions into the domain before the first hits the upper boundary. The modulo function mod is used to simulate the z -dependence of the

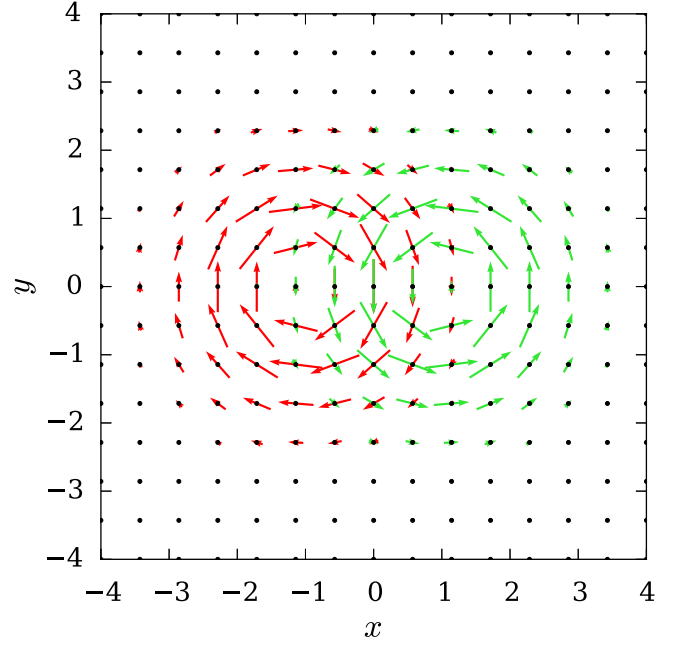


Figure 3. Representation of the footpoint driving velocity at two different times in red (left) and green (right) arrows. We switch between the two driving vortices every 32 code units.

magnetic field. More precisely, it is given as

$$\pm = \begin{cases} + & \text{if } \text{mod}(\text{int}(t/t_{E3}), 2) = 0 \\ - & \text{if } \text{mod}(\text{int}(t/t_{E3}), 2) \neq 0 \end{cases} \quad (12)$$

with the integer function int. In Figure 3 we plot a representation of the driver at two different times with twist injections on the left and right half of the domain.

For our driver we have in mind a setting at the lower part of the corona with lower densities such that back-reactions from the magnetic field to the fluid can be significant. Furthermore, any direct imposition of the velocity at the lower boundary would create a strong shear between the boundary and the first inner layer of the simulation box. Therefore, we force the plasma velocity \mathbf{u} toward the velocity \mathbf{u}_d at $z = z_0$ through an exponential saturation of the form

$$\frac{\partial \mathbf{u}}{\partial t} = (\mathbf{u} - \mathbf{u}_d) / \lambda_u, \quad (13)$$

with the saturation half time λ_u . We choose $\lambda_u = 0.3$ for the homogeneous case and $\lambda_u = 0.01$ for the other two test cases, which ensures a reasonably fast saturation for the velocity. Note that due to its nature, the driver can be also counteracted by forces from the magnetic field. This back-reaction depends on the geometry of the field and can lead to a nonsaturating velocity.

2.7. Magnetic Skeleton

We expect the magnetic topology to undergo drastic changes due to the boundary driver. The magnetic skeleton, which comprises the stable and unstable manifolds connected to magnetic null points, characterizes the magnetic topology and separates the domain into regions of different magnetic connectivity. Hence, the emergence or annihilation of magnetic nulls in the domain indicates major changes in the magnetic

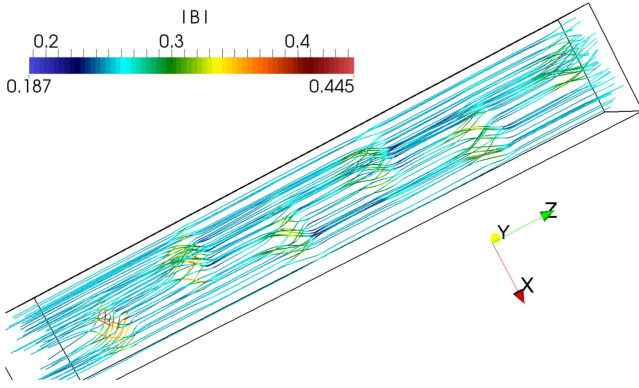


Figure 4. Magnetic field lines for the initially homogeneous case at $t = 192$, where the colors denote the field strength $|B|$.

topology. Magnetic null points may merge or be created in pairs—in each case one null of the pair must have topological degree $+1$ and the other topological degree -1 (Fukao et al. 1975; Greene 1988; Hornig & Schindler 1996; Murphy et al. 2015). They can also appear through the boundary, which is essentially open to magnetic flux. As a result, separatrix surfaces, which separate areas of different magnetic connectivity, may appear and disappear within the volume during the evolution. Since the processes of null pair creation/annihilation require a nonideal evolution, they are of interest in understanding reconnection and heating in the volume (Wyper & Pontin 2014; Murphy et al. 2015; Olshevsky et al. 2015). We therefore analyze the evolution of the magnetic skeleton during the simulations.

We find the magnetic nulls in our simulations using the trilinear extrapolation of the magnetic field, which assumes a sufficiently linearizable field at subgrid scale (Haynes & Parnell 2007). To find the separatrix surfaces, we use the ring method (which can be found in, e.g., Haynes & Parnell 2010), in which we trace magnetic field lines from points around the magnetic nulls. Similarly, we find the spines corresponding to the fan separatrix surfaces by tracing out magnetic field lines.

3. RESULTS

3.1. Injection of Braiding

As a proof of concept we inject the E^3 braid (Wilmot-Smith et al. 2009) into the initially homogeneous field region using the prescribed driver (Equations (9)–(13)) and the parameter $u_0 = 0.5$.

As we expect, the disturbances from the footpoint motion travel into the domain via (torsional) Alfvén waves. This leads to a buildup of twisting regions that move into the domain. As the end result we obtain a magnetic field configuration that resembles the expected E^3 braid (Figure 4). This illustrates the efficacy of the footpoint motions to change the topology of the magnetic field in the case where all field lines are “open,” so that disturbances propagate freely into the domain until they reach the top boundary.

Through magnetic resistivity the field is subject to dissipation, which can lead to small changes of the field-line topology even in the absence of intense current layers. In order to track this, we compute the field-line mapping given as the mapping of points (x, y) from the $z = z_0$ plane to the upper boundary $F(x, y)$, which

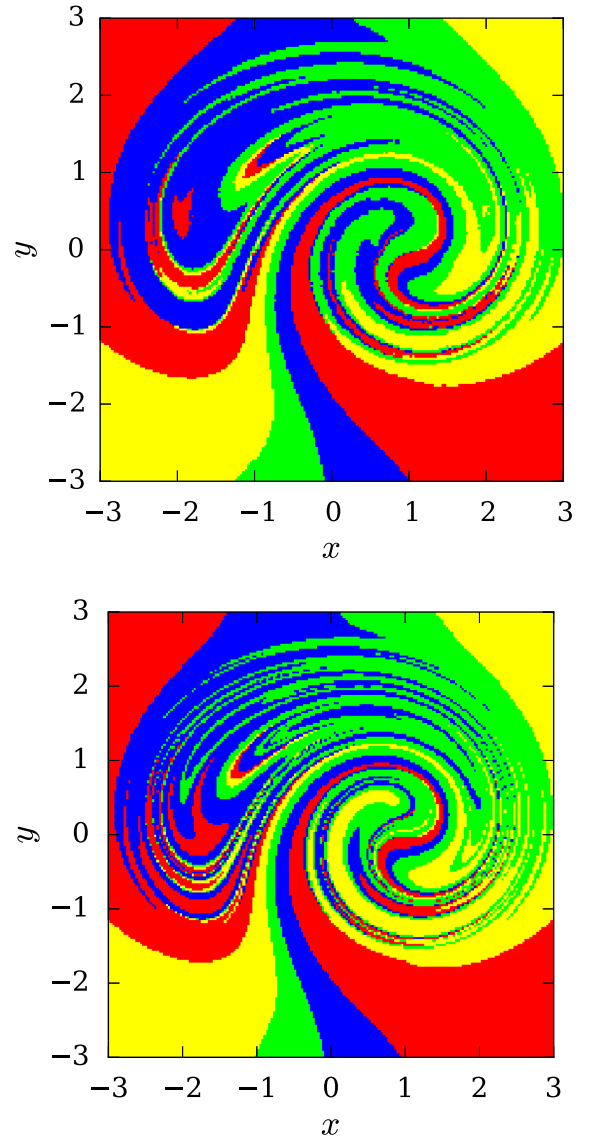


Figure 5. Color map for the homogeneous field at $t = 192$ (upper panel) and for the exact E^3 field (lower panel).

is induced by the magnetic field lines (Yeates et al. 2010). We then use this mapping to compute the color mapping, where we assign the colors red, blue, green, and yellow for $(F_x > x) \wedge (F_y > y)$, $(F_x > x) \wedge (F_y < y)$, $(F_x < x) \wedge (F_y < y)$, and $(F_x < x) \wedge (F_y > y)$, respectively (Figure 5).

After time $t = 192$ the field has undergone sufficient braiding to correspond in the ideal limit to the E^3 braid. We compare the color mapping of our final magnetic field with the color mapping of the exact E^3 field shown in Figure 2 of Yeates et al. (2010) and find a striking agreement. The small differences are due to the small but finite magnetic resistivity, which leads to magnetic field dissipation. The resulting field is then topologically somewhat simpler than the exact E^3 braid presented by Yeates et al. (2010).

For the two magnetic carpet structures with magnetic nulls and separatrix layers, the propagation of the boundary motions is significantly restricted by the field topology. Many of the field lines that have footpoints within the twisting regions close back to the lower boundary rather than extending to the upper

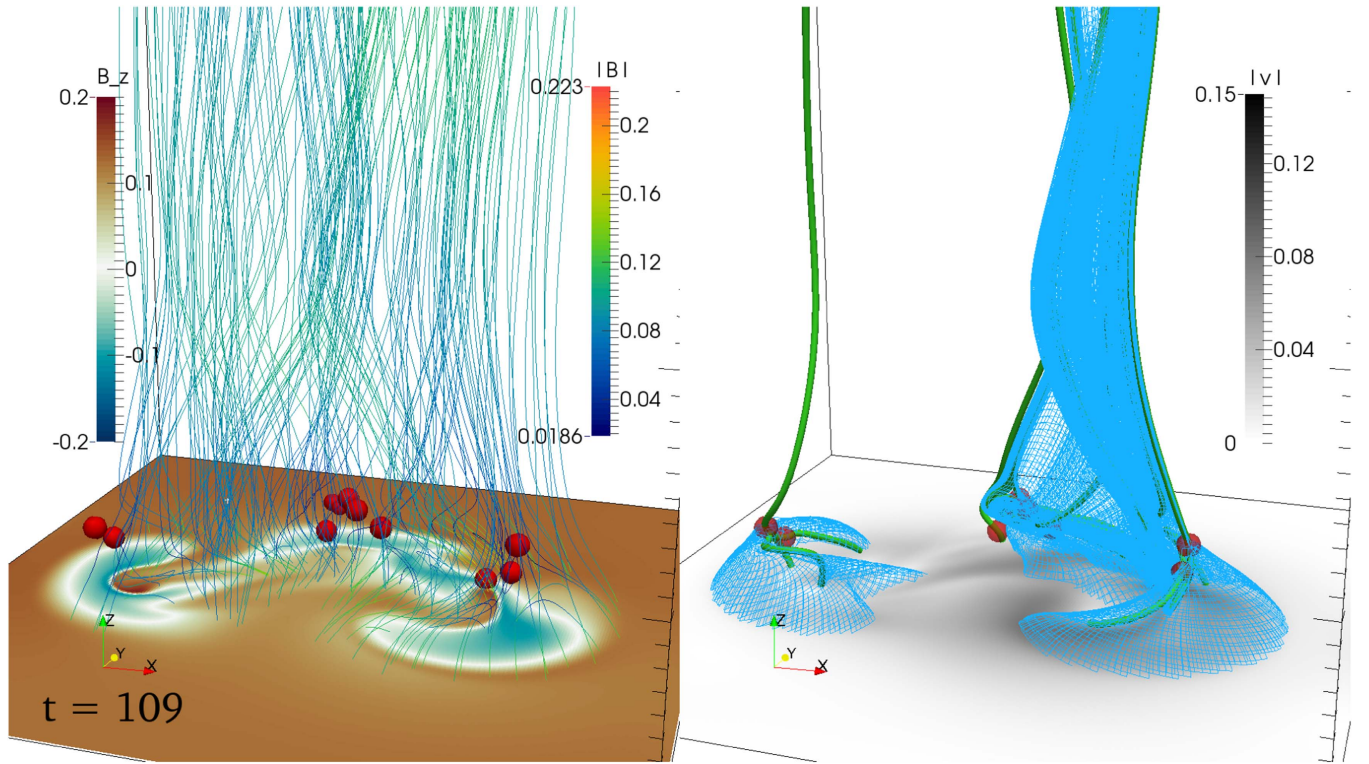


Figure 6. Magnetic field lines (left) for the parasitic polarities case at $t = 109$, where the colors denote the field strength $|\mathbf{B}|$ together with the null points (red spheres) and the z -component of the magnetic field at the lower boundary. The right panel shows the magnetic skeleton with the null points (red spheres), magnetic spines (green tubes), and separatrix surfaces (blue grid surface), together with the magnitude of the velocity at the lower boundary.

(An animation of this figure is available.)

boundary. This leads to Alfvénic waves traveling back to the photosphere and a buildup of magnetic stresses at low altitudes. However, as the forcing continues, the magnetic carpet structure is disrupted, as described in the following section, reducing the fraction of the driving region covered by closed magnetic field lines, and thus allowing a propagation of the Alfvénic waves to higher altitudes (Figure 6). We quantify this in Section 3.5, where we measure the magnetic energy propagation in the different cases.

3.2. Magnetic Carpet and Field Topology

As the magnetic carpet gets forced from the photosphere, the magnetic field topology undergoes various changes. We observe the creation and annihilation of pairs of nulls, and sometimes also the surfacing of nulls through the photosphere. While the former has been observed in the past (e.g., Maclean et al. 2009; Wyper & Pontin 2014; Murphy et al. 2015; Olshevsky et al. 2015), the latter is a rather unstudied phenomenon in MHD simulations (though see Brown & Priest [2001] for a magnetic charge topology model). It turns out that through its particular evolution at the surface, the field is being restructured in such a way that it gives rise to additional magnetic nulls and a rather complex structure of the separatrix surfaces (Figure 6).

As new nulls appear in the domain, the configurations of the separatrix surfaces and the spines change as well. Considering first the case of embedded parasitic polarities, we observe that at an early time (ca. $t = 40$ in video1) in the simulation a null point appears through the lower boundary, between the central and right separatrix domes. That gives rise to a separator pair

connecting the new null to both the central and right null points. The separatrix surface of this new null point is bounded by the spines of the original right and central nulls. Therefore, part of it extends down to the photospheric boundary, while another part extends up to the top of the box. Such a structure is often called a “separatrix curtain” (Titov et al. 2011), and we see many of these appear and disappear during the evolution (see Figure 6 and video1) as the null point bifurcations occur. Apart from such emerging and submerging of single nulls, we also observe the annihilation and creation of pairs of nulls with opposite sign in the weak-field region surrounding the original nulls (see Figure 6), as predicted by Greene (1988), Albright (1999), and Wyper & Pontin (2014).

The dynamics of the magnetic null points becomes clearer by computing the average height of the null points and the number of null points as a function of time (Figure 7). The first thing that we observe is that for the parasitic polarity case the number of null points is much more highly fluctuating, while for the dominant polarity case the null points are more stable. For the parasitic polarity case we have bursty production of nulls until $t \approx 100$ (both through topological bifurcations within the domain and null emergence through the photosphere, as described above). After this time there is a sharp drop in the average height of the nulls as a result of the shredding of the polarities, and concurrent with this, the null point number drops rapidly as many nulls leave through the lower boundary. The number of null points and their average height are intimately linked with the fraction of the photospheric flux that is “open” to the upper boundary, thus having important implications for the propagation of energy and

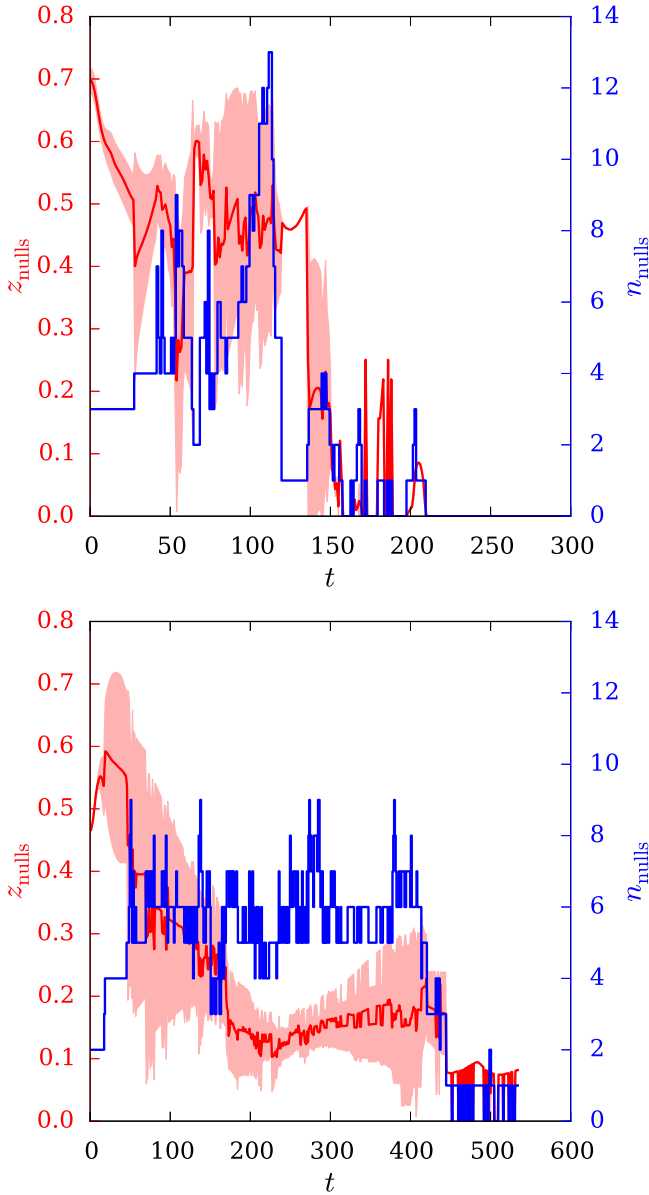


Figure 7. Average height of the null points z_{nulls} (red line) with standard deviation (light-red shading) together with the total number of magnetic null points n_{nulls} (blue line) as a function of time for the parasitic polarity case (upper panel) and dominant polarity case (lower panel).

disturbances from the lower boundary to higher altitudes. This will be discussed further below.

The above analysis provides a qualitative picture of the propagation of disturbances into the corona in response to the footpoint motions. In the following sections we go on to discuss quantitative measures such as energy and helicity fluxes.

3.3. Helicity Injection

From Equation (7) we know that magnetic energy can be injected from the boundary as long as the velocity is not perfectly orthogonal to the magnetic field and \mathbf{B} is not perpendicular to the surface normal. For the homogeneous configuration this is the case initially. However, after the first movement of the footpoints, this changes: energy injection is

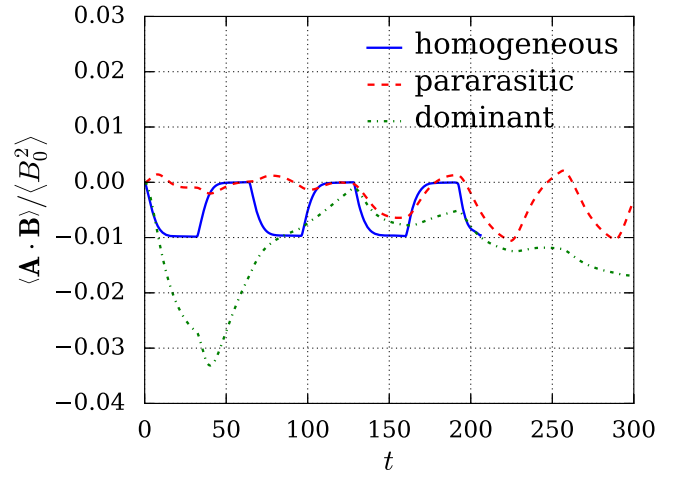


Figure 8. Time evolution of the normalized magnetic helicity for the three different configurations.

possible, and disturbances of the field propagate through Alfvénic waves into the domain.

The initially homogeneous field is easily being twisted by the footpoint motions, which leads to the injection of magnetic helicity for every odd multiple of t_{E3} . We clearly observe this behavior in Figure 8. On the other hand, the cases of parasitic and dominant polarities with their intricate structure and closed (to the photosphere) field lines inhibit any such propagation initially. As a consequence, magnetic helicity is not efficiently injected into the domain. However, after sufficient twisting, the field realigns itself to a simpler structure, which then allows for efficient propagation of boundary disturbances to large heights. For that to happen the field needs to reconnect, which is forced by the footpoint motions.

3.4. Energy Fluxes, Conversion, and Dissipation

We now calculate the individual contributions to the change in time of the kinetic and magnetic energy for the embedded parasitic polarity and the dominant polarity case by applying Equations (7) and (8). Since the wave damping region at $z > 8$ lies conceptually outside the physical domain of interest, we perform the integrals within $z \leq 8$.

It is clear from Figure 9 for the embedded polarity case that magnetic energy is injected through the lower boundary. From there it propagates into the domain, where it is mostly converted into kinetic energy through the Lorentz force. At later times magnetic energy injection and conversion reach an approximate equilibrium.

How is the magnetic energy dissipated? Judging from the results (Figure 9), the channel through ohmic dissipation ηJ^2 is rather limited due to the low value of η compared to the energy input from the photosphere. Similarly, other forms of magnetic energy fluxes are negligible compared to the energy injection rate, like the Poynting flux through the upper domain boundary and magnetic energy advection. However, after conversion into kinetic energy, viscous effects are efficient enough to account for a large part of the energy dissipation.

For the embedded dominant polarity case we first have to account for effects coming from the small nonpotentiality of this configuration near the lower boundary. To achieve this, we perform a simulation without boundary driver and subtract the values of the driven simulation from the values with $\mathbf{u}_d = 0$.

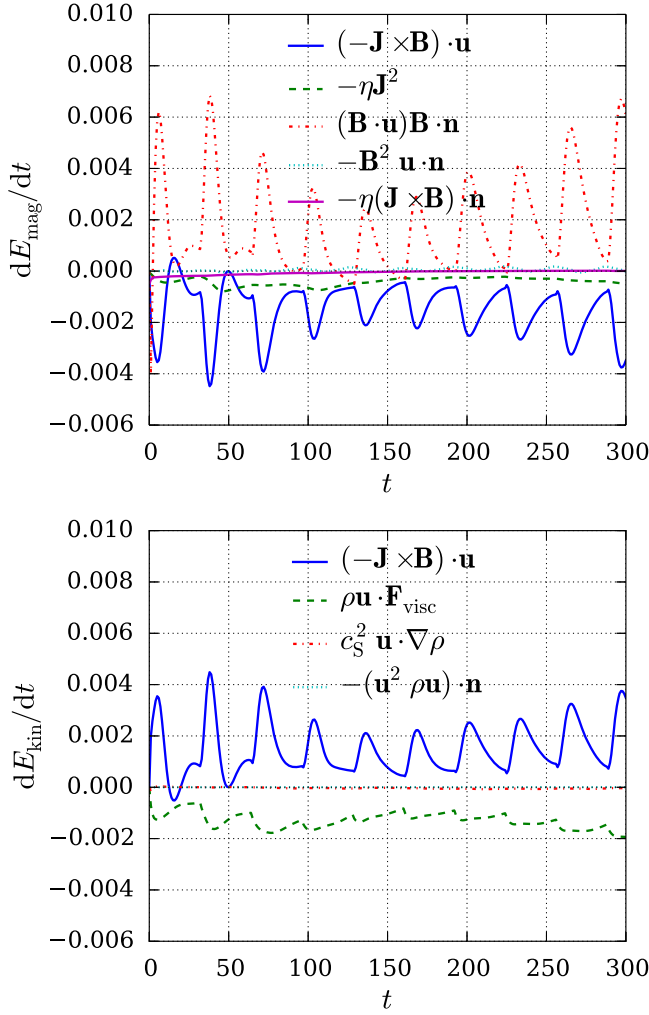


Figure 9. Time evolution of the contributions to the magnetic energy change (upper panel) and kinetic energy change (lower panel) for the embedded parasitic polarity initial condition. Note that for the first two quantities in the list for the magnetic energy and the first three quantities for the kinetic energy what we plot are the volume integrals, where the volume is taken as the computational domain excluding the wave damping region. Terms involving the normal vector \mathbf{n} are integrated over the surface of this volume.

However, these effects become negligible after $t \approx 15$. We then observe a rather large release of magnetic energy, which is converted into kinetic energy (Figure 10). This is due to the strong field close to the photosphere at $z = z_0$. The conversion and dissipation channels are the same as for the embedded polarity case, i.e., magnetic energy is converted into kinetic energy through the Lorentz force and then mostly dissipated through viscous effects. Over time we also observe a clear decrease for all terms, which is due to the change of a strong near-surface field into a more homogeneous and weaker field as the initial polarity regions are distorted and ultimately spread out by a combination of the boundary flows and diffusion.

3.5. Propagation of Energy to Higher Altitudes

For the initially homogeneous field any energy or information is transported through Alfvénic waves, while acoustic waves appear to be insignificant. Any magnetic field disturbance propagates freely into the domain (Figure 11), with the Poynting flux carrying the energy. Due to the small

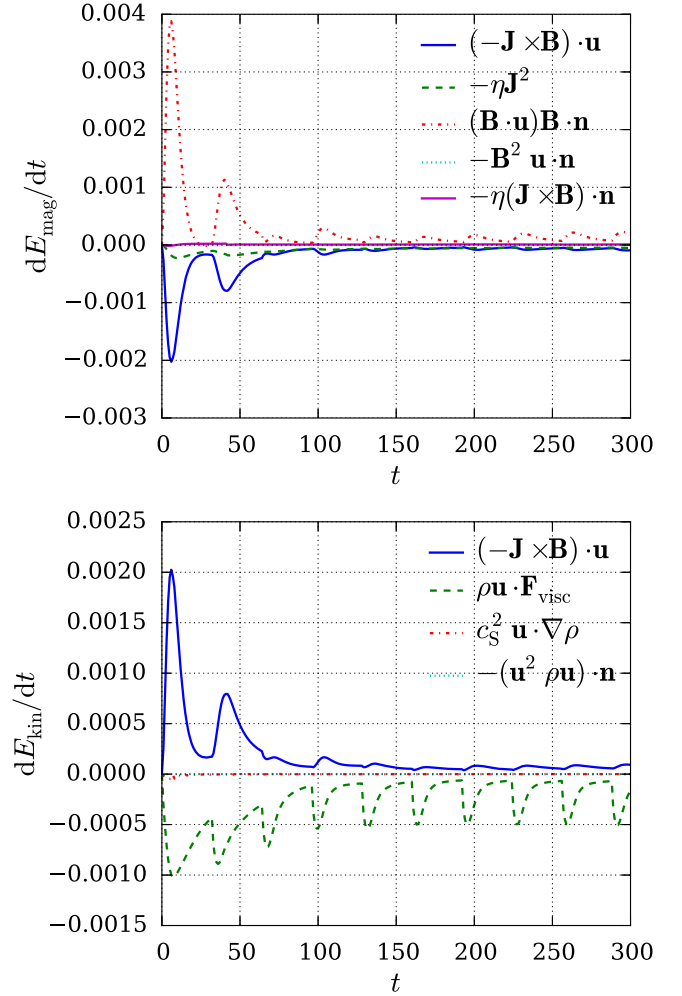


Figure 10. Time evolution of the contributions to the magnetic energy change (upper panel) and kinetic energy change (lower panel) for the dominant polarity initial condition. Volume and surface integrals are taken as appropriate, as in Figure 9.

value of the magnetic resistivity η and viscosity ν , the Alfvénic waves are only marginally damped, such that the energy is efficiently transported to the top of the domain. Since for this case the upper boundary allows for the reflection of Alfvénic waves, we stop the simulation as soon as the first wave packet reaches the boundary.

For the parasitic polarity configuration the energy from the footpoint motion is initially trapped at low heights (Figure 12), primarily below the null points and the separatrix domes. This is due to the trapping of Alfvénic waves through closed (to the photosphere) magnetic field lines. For $100 \leq t \leq 200$, we observe a restructuring of the magnetic skeleton, as described in Section 3.2, which is characterized by a shrinking of the domes as the parasitic polarities are “shredded” by the photospheric flows. This leads to a flux of magnetic null points through the lower boundary and their subsequent disappearance (Figure 7). As a result, there is now a larger fraction of the field lines at the photosphere that are open, allowing the injected twist to travel into the domain. Note that the increase in efficiency of energy propagation to large heights coincides with the disappearance of the magnetic null points at time $t \approx 210$.

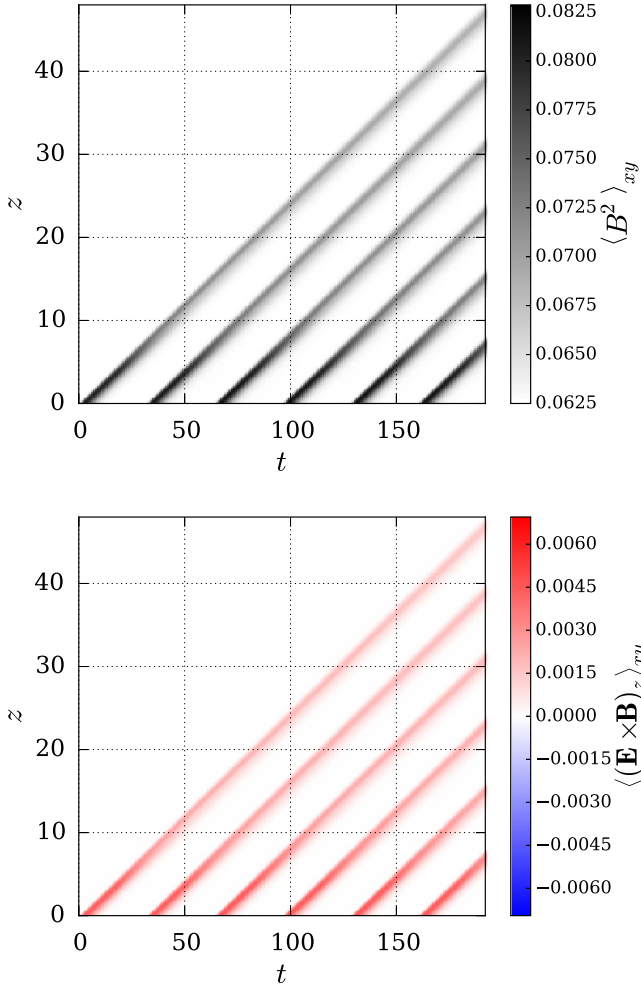


Figure 11. Averages in the xy -plane of B^2 and the Poynting flux in the z -direction $(\mathbf{E} \times \mathbf{B})_z$ as a function of the vertical coordinate z and time t for the initially homogeneous case.

Similarly, for the dominant polarity case we observe a trapping of magnetic energy below the locations of the magnetic nulls. Due to the strong field, most of the magnetic energy is stored close to the photosphere. This holds until the breakage of the field's topology into a simpler structure that allows for fluxes into the domain. Therefore, we observe energy fluxes after time $t \approx 200$ that more easily reach the top boundary (Figure 13). We quantify the efficiency of the propagation via the ratio of the Poynting flux at $z = 2$ to the value at $z = 0$. Since the Alfvén speed varies with height, we take the values at $z = 2$ with a time delay of 100 code time units, which gives us a reasonably good estimate. By doing so, we find a ratio for the Poynting flux of ca. 0.35% for waves emitted at $t = 64$ and a ratio of 2.8% for $t = 415$. This shows that the energy flux is enhanced after the breakup of the magnetic field topology.

4. DISCUSSION AND CONCLUSIONS

We have considered above the application of boundary flows to three different model coronal fields. In the first, most simplified model an initially homogeneous field was used. In this case we showed that it is feasible to induce braiding to the magnetic field of the solar corona by motions on the

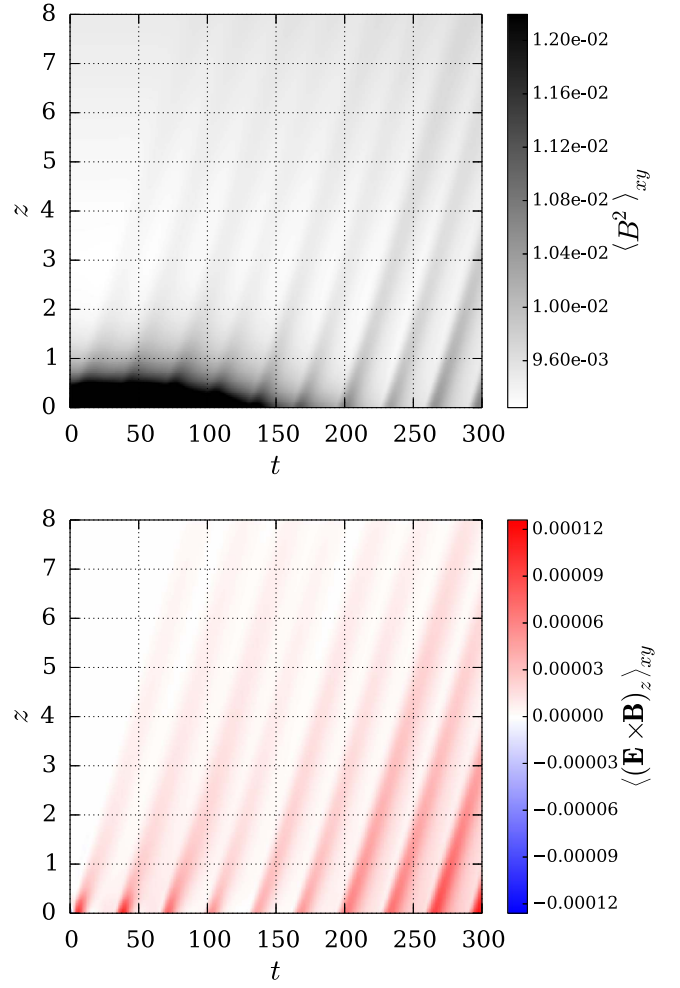


Figure 12. Averages in the xy -plane of B^2 and the Poynting flux in the z -direction $(\mathbf{E} \times \mathbf{B})_z$ as a function of the vertical coordinate z and time t for the parasitic polarity case.

photosphere. Moving to the more realistic models with a mixed polarity photospheric field, the energy transport to large altitudes was inhibited by the complex field topology. In this work we did not include a stratified atmosphere in which the Alfvén speed can change by several orders of magnitude. It was shown by van Ballegoijen et al. (2014) that this has a strong effect on the propagation and dissipation of energy and should therefore be considered in a future study. While for large Alfvén speeds, compared to the driving velocities, the DC heating dominates, for small Alfvén speeds AC dominates. Furthermore, nonlinear effects lead to the dissipation of counterpropagating waves.

In order to understand our results in the context of the corona, we can extract synthetic magnetograms of the line-of-sight magnetic field from the magnetic field on the lower boundary of our simulation domain and compare with processes occurring in observed solar magnetograms. Here we take the line of sight to be simply the z -direction. In order to compare with actual observations, we reduce the z -component of the magnetic field to three values. Specifically, it is set to $+1$ at points where $B_z(z=0) > B_{\text{cut}}$, -1 if $B_z(z=0) < -B_{\text{cut}}$, and 0 otherwise (to simulate the noise threshold on magnetogram observations). For the parasitic polarity case, shown in Figure 14, we choose $B_{\text{cut}} = 0.15 \times |B_z(x, y, z=0, t)|_{\text{max}}$, and for the dominant

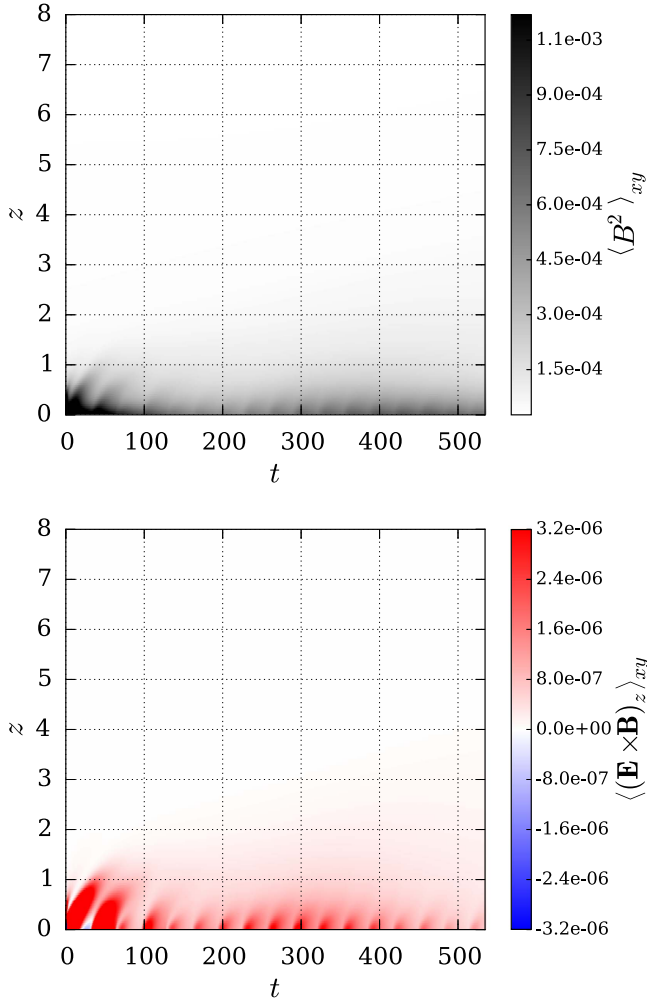


Figure 13. Averages in the xy -plane of B^2 and the Poynting flux in the z -direction $(\mathbf{E} \times \mathbf{B})_z$ as a function of the vertical coordinate z and time t for the dominant polarity case.

polarity case we choose $B_{\text{cut}} = 0.003 \times |B_z(x, y, z = 0, t)|_{\text{max}}$ (Figure 15). Note that we take the maximum over x , y , and t , which means that the cutoff value is fixed in time.

From the synthetic magnetograms for both simulations we clearly observe a complex interaction of opposite polarity regions, which may lead to both the splitting and merging of polarity regions (sometime called “flux fragments”). At later times, however, due to the overall mixing and cancellation of the polarities (a result of both the stretching nature of the imposed flow and diffusion), we end up with one surviving polarity region (positive). This behavior is consistent with the observed behavior of magnetic flux fragments on the Sun, which are known to undergo a continuous process of merging and fragmentation (e.g., DeForest et al. 2007, and references therein). It is important to note that this “shredding” of the magnetic flux fragments in the synthetic magnetograms is crucially dependent on the relative length scales of the flows and the flux fragments; in our case the flows have significant gradients over the scale of the initial fragments. From this point of view, our results are probably best compared to local regions of the photosphere in which the flux fragments are comparable to the scale of the underlying motions (Gošić et al. 2014).

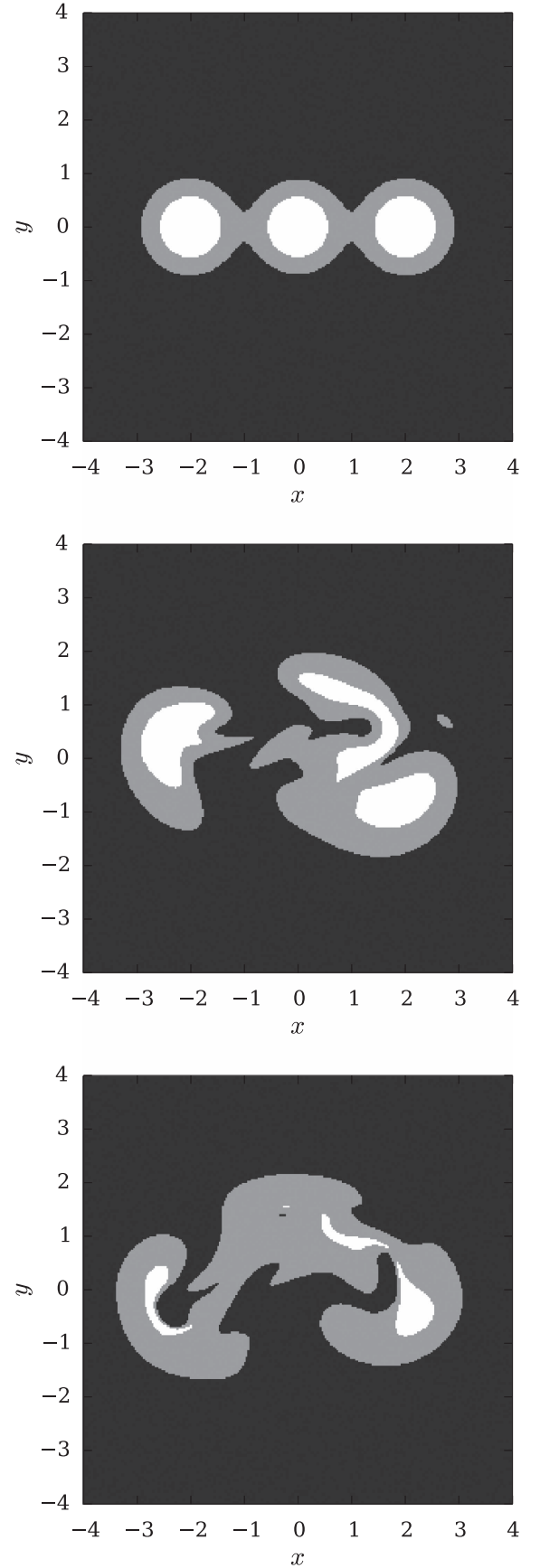


Figure 14. Synthetic magnetogram for the parasitic polarity case at times $t = 0$ (upper panel), $t = 58$ (middle panel), and $t = 109$ (lower panel). The shadings correspond to the reduced z -component of the magnetic field, with black positive and white negative polarity.

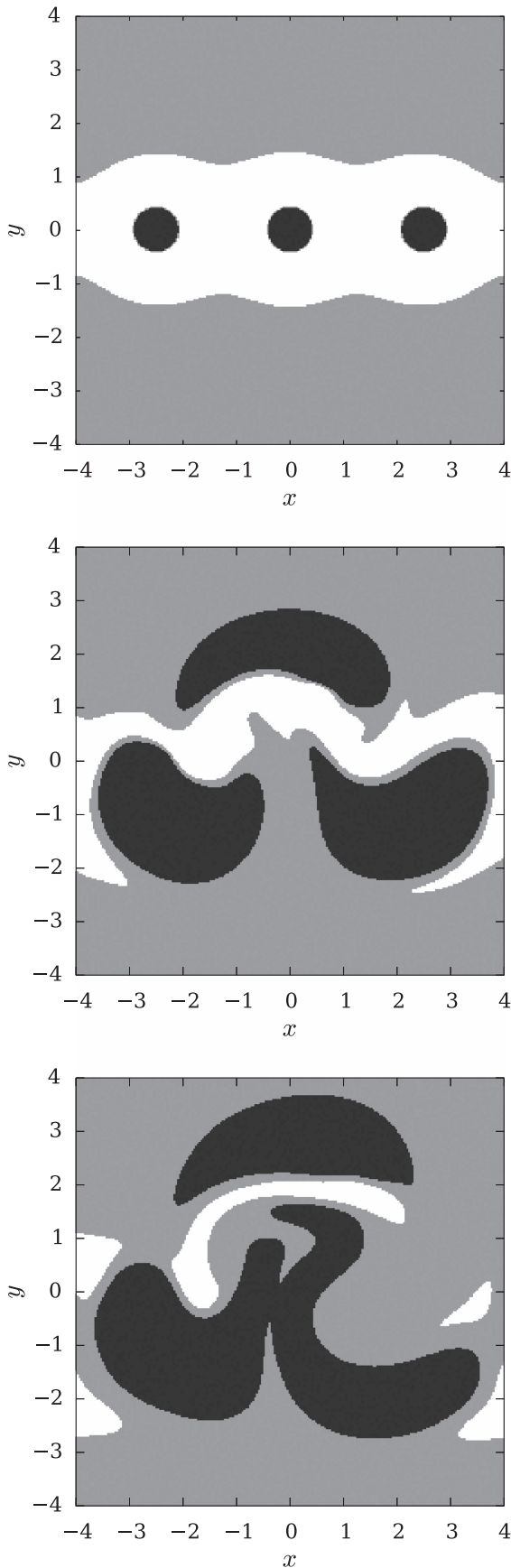


Figure 15. Synthetic magnetogram for the dominant polarity case at times $t = 0$ (upper panel), $t = 95$ (middle panel), and $t = 185$ (lower panel). The shadings correspond to the reduced z -component of the magnetic field, with black positive and white negative polarity.

In the two models with embedded parasitic/dominant polarities, we investigated the effects of footpoint motions on fields where a significant fraction of the field lines initially connect back to the photosphere, while others connect to the upper boundary. The applied photospheric motions do not create new magnetic flux, but, as discussed above, induce shredding of existing flux, leading in the magnetograms to the eventual “death” of the flux fragments (Lamb et al. 2013). On the Sun, this process is in a statistically steady state with the competing process of emergence of new flux—which we exclude from our simplified model.

We showed that in the initial stages of the simulations with mixed polarity, the presence of closed field lines restricted the energy propagation into the domain. However, as we continue with the driving, the embedded polarities are shredded into weaker fragments. This reduces the range over which they influence the coronal field. In particular, we have shown that it results in a reduction in the number, and perhaps more importantly the height, of the coronal null points. This is particularly clear in the case of the embedded parasitic polarities, where the separatrix domes enclosing the closed flux get progressively smaller (on average, both in height and in extent over the xy -plane) as the simulation proceeds. As a result, the propagation of disturbances can access the open-field regions more readily, and the energy is propagated much more efficiently to large heights.

In summary, we can confirm the feasibility of energy and disturbance propagation from the photosphere into the corona through the motion of footpoints. The magnetic field topology plays an essential role during this process, with a magnetic carpet structure containing nulls largely inhibiting the process. We showed that the shredding of magnetic polarities by photospheric flows leads to a simplification of the magnetic topology through the disappearance of null points (either through the lower boundary or in annihilation processes within the volume). This in turn allows a more effective propagation of energy to large heights in the corona.

All the authors acknowledge financial support from the UK’s STFC (grant no. ST/K000993). We also thank the anonymous referee for the useful comments that helped improve this paper.

REFERENCES

- Albright, B. J. 1999, *PhPl*, **6**, 4222
Aulanier, G., Parlat, E., & Démoulin, P. 2005, *A&A*, **444**, 961
Bingert, S., & Peter, H. 2011, *A&A*, **530**, A112
Bogdanov, S. Y., Burilina, V. B., Markov, V. S., & Frank, A. G. 1994, *JETPL*, **59**, 537
Brandenburg, A., & Dobler, W. 2002, *CoPhC*, **147**, 471
Brown, D. S., & Priest, E. R. 2001, *A&A*, **367**, 339
De Moortel, I., & Galsgaard, K. 2006, *A&A*, **459**, 627
DeForest, C. E., Hagenaar, H. J., Lamb, D. A., Parnell, C. E., & Welsch, B. T. 2007, *ApJ*, **666**, 576
Démoulin, P., Bagala, L. G., Mandrini, C. H., Hénoux, J. C., & Rovira, M. G. 1997, *A&A*, **325**, 305
Edwards, S., & Parnell, C. 2015, *SoPh*, **290**, 2055
Effenberger, F., & Craig, I. 2015, *SoPh*, **291**, 143
Filippov, B. 1999, *SoPh*, **185**, 297
Fukao, S., Ugai, M., & Tsuda, T. 1975, *Rep. Ionos. Space Res*, **29**, 133
Galsgaard, K., Parnell, C. E., & Blaizot, J. 2000, *A&A*, **362**, 395
Gošić, M., Rubio, L. R. B., Suárez, D. O., Katsukawa, Y., & del Toro Iniesta, J. C. 2014, *ApJ*, **797**, 49
Greene, J. M. 1988, *JGR*, **93**, 8583
Gudiksen, B. V., & Nordlund, Å. 2005, *ApJ*, **618**, 1031
Haynes, A. L., & Parnell, C. E. 2007, *PhPl*, **14**, 8
Haynes, A. L., & Parnell, C. E. 2010, *PhPl*, **17**, 9
Hornig, G., & Schindler, K. 1996, *PhPl*, **3**, 781

- Lamb, D. A., Howard, T. A., DeForest, C. E., Parnell, C. E., & Welsch, B. T. 2013, [ApJ](#), **774**, 127
- Larmor, S. J. 1934, [MNRAS](#), **94**, 469
- Lau, Y.-T., & Finn, J. M. 1990, [ApJ](#), **350**, 672
- Longcope, D. W., Brown, D. S., & Priest, E. R. 2003, [PhPl](#), **10**, 3321
- Maclean, R. C., Parnell, C. E., & Galsgaard, K. 2009, [SoPh](#), **260**, 299
- Mellor, C., Gerrard, C., Galsgaard, K., Hood, A. W., & Priest, E. R. 2005, [SoPh](#), **227**, 39
- Murphy, N. A., Parnell, C. E., & Haynes, A. L. 2015, [PhPl](#), **22**, 10
- Olshevsky, V., Divin, A., Eriksson, E., Markidis, S., & Lapenta, G. 2015, [ApJ](#), **807**, 155
- Platten, S. J., Parnell, C. E., Haynes, A. L., Priest, E. R., & Mackay, D. H. 2014, [A&A](#), **565**, A44
- Pontin, D. I. 2011, [AdSpR](#), **47**, 1508
- Pontin, D. I., Bhattacharjee, A., & Galsgaard, K. 2007, [PhPl](#), **14**, 5
- Pontin, D. I., & Craig, I. J. D. 2005, [PhPl](#), **12**, 072112
- Priest, E. R., Heyvaerts, J. F., & Title, A. M. 2002, [ApJ](#), **576**, 533
- Ritchie, M. L., Wilmot-Smith, A. L., & Hornig, G. 2016, [ApJ](#), **824**, 19
- Santamaria, I. C., Khomenko, E., & Collados, M. 2015, [A&A](#), **577**, A70
- Schrijver, C. J., DeRosa, M. L., & Title, A. M. 2010, [ApJ](#), **719**, 1083
- Schrijver, C. J., Title, A. M., Harvey, K. L., et al. 1998, [Natur](#), **394**, 152
- Titov, V. S., Mikić, Z., Linker, J. A., Lionello, R., & Antiochos, S. K. 2011, [ApJ](#), **731**, 111
- van Ballegoijen, A. A., Asgari-Targhi, M., & Berger, M. A. 2014, [ApJ](#), **787**, 87
- Wilmot-Smith, A. L., Hornig, G., & Pontin, D. I. 2009, [ApJ](#), **696**, 1339
- Wyper, P. F., & Pontin, D. I. 2014, [PhPl](#), **21**, 102102
- Yeates, A. R., Hornig, G., & Wilmot-Smith, A. L. 2010, [PhRvL](#), **105**, 085002